

# Ultrasonic positioning system for the calibration of central detector

Guo-Lei Zhu<sup>1</sup> · Jiang-Lai Liu<sup>2</sup> · Qi Wang<sup>1</sup> · Meng-Jiao Xiao<sup>3,4</sup> · Tao Zhang<sup>2</sup>

Received: 4 May 2018 / Revised: 13 June 2018 / Accepted: 20 July 2018 / Published online: 2 January 2019

© China Science Publishing & Media Ltd. (Science Press), Shanghai Institute of Applied Physics, the Chinese Academy of Sciences, Chinese Nuclear Society and Springer Nature Singapore Pte Ltd. 2019

**Abstract** A thorough detector response calibration using radioactive sources is necessary for the Jiangmen Underground Neutrino Observatory. Herein, we discuss the design of a source positioning system based on ultrasonic technology, aiming for a 3-cm precision over the entire 35-m diameter detector sphere. A prototype system is constructed and demonstrated for the experiment.

**Keywords** JUNO · Calibration · Ultrasonic positioning

## 1 Introduction

The Jiangmen Underground Neutrino Observatory (JUNO) [1] is being developed to study the neutrino mass hierarchy [2–4] using a large underground liquid scintillator (LS) detector in Guangdong, China. The central

detector (CD) is enclosed in an acrylic sphere with an inner diameter of 35.4 m and a thickness of 12 cm, which contains approximately 20,000 tons of LS [5–7]. The CD is covered by approximately 17,000 and 25,000 20-inch and 3-inch photomultipliers (PMTs), respectively [8, 9], located in an outer layer of ultrapure water to reach > 75% photocathode coverage. For this large detector, the neutrino mass hierarchy can be determined by performing accurate measurements on the reactor neutrino energy spectrum at a baseline of approximately 53 km with an unprecedented energy resolution (approximately 3% at 1 MeV of detected energy) and excellent energy scale uncertainty (< 1%) [10, 11]. To address both requirements, a thorough calibration program is designed to deploy multiple radioactive or optical calibration sources to a wide range of positions inside the CD. The automated deployment systems are the following four: automatic calibration unit (ACU, central axis, similar to Daya Bay's design [12, 13]), cable loop system (CLS, one vertical plane), remote operate vehicle (ROV,  $4\pi$ ), and guide tube (GT, one loop on the outer circumference of the CD). See Fig. 1 for the overall schematics [14]. In all these systems, the location of the source is required to be known to a few centimeters. For the ACU and GT, the source deployment is confined by the gravity and a tube, respectively. Therefore, the source position can be determined accurately by the length of the cables. For the CLS, effects such as the self-weight of the cable, buoyance force, internal tension result in an inaccuracy of source locations based on the cable lengths alone, in particular for locations near the boundary. The remotely operated vehicle (ROV) has even more freedom as it is driven by its internal jet pumps. Thus, a dedicated positioning system serving both the CLS and ROV is required.

---

This work was supported by the “Strategic Priority Research Program” of the Chinese Academy of Sciences (No. XDA10010800) and the “Fundamental Research Funds for the Central Universities” (No. 3102017zy010).

---

✉ Qi Wang  
qwang208@nwpu.edu.cn

<sup>1</sup> School of Marine Science and Technology, Northwestern Polytechnical University, Xi'an 710072, China

<sup>2</sup> Shanghai Laboratory for Particle Physics and Cosmology, INPAC and School of Physics and Astronomy, Shanghai Jiao Tong University, Shanghai 200240, China

<sup>3</sup> Department of Physics, University of Maryland, College Park, MD 20742, USA

<sup>4</sup> Center of High Energy Physics, Peking University, Beijing 100871, China

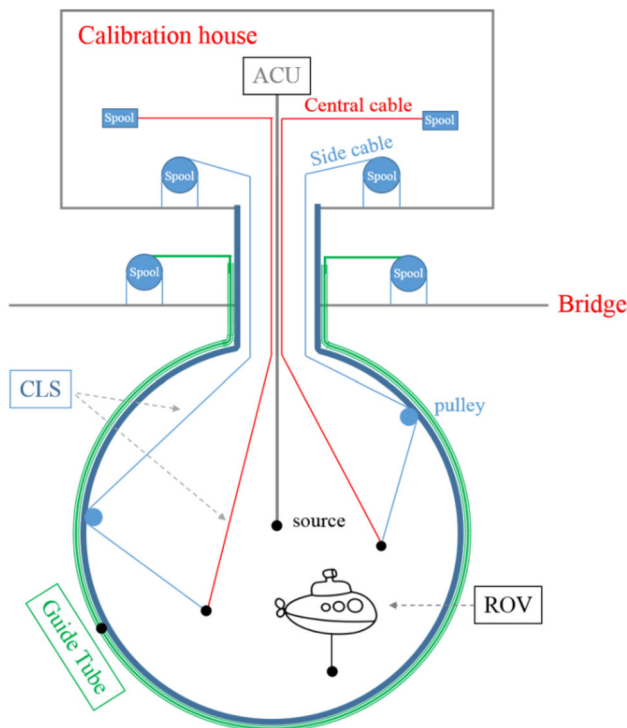


**Fig. 1** (Color online) Overall schematics of calibration deployment system

We herein report the design of an ultrasonic positioning system, with emitters located on the CLS and ROV, and receivers fixed in the CD. The remainder of this paper is organized as follows. The requirements are discussed in Sect. 2, followed by a brief description of the working principle in Sect. 3. In Sect. 4, the technical design of the system is discussed. The construction and performance of a prototype system is detailed in Sect. 5, followed by concluding remarks in Sect. 6.

## 2 Requirements and technical choice

According to preliminary Monte Carlo simulations, the resolution of the event vertex reconstruction based on JUNO PMTs alone can achieve a level of 10 cm [1, 13]. This is important because a fiducial volume cut is envisioned to remove the peripheral background events. As a key physical requirement, the positioning system must determine the location of the source to better than 5 cm in the entire 35-m detector sphere, to serve an unbiased control of the vertex reconstruction. It must also operate without maintenance for 20 years, thus placing a strong requirement on the simplicity of the underwater component.

Owing to the complication of the optical interfaces between the LS ( $n = 1.48$ ), acrylic ( $n = 1.48$ ), and water

( $n = 1.33$ ), an optical-image-based system (e.g., CCD) would bear the positioning uncertainties, particularly when the source moves closer to the boundary. Furthermore, the lighting for the cameras and the detector PMTs cannot be operated simultaneously, which further restricts its usage. Meanwhile, using an ultrasonic system with highly reliable piezoelectric components is a standard practice in marine engineering. Being acoustic, ultrasonic signals are fully compatible with the PMT operation. Additionally, if the receivers are located inside the LS, the acoustics can be simple without boundary effects. Typical ultrasonic waves have a frequency of 100 kHz, with an intrinsic resolution up to its wavelength (13.8 mm in the LS). Therefore, in the baseline design, we attached the ultrasonic emitters to the radioactive source in the CLS and ROV, and the receivers were fixed as an array on the inner acrylic wall. This design leads to two more requirements, (a) being inside the LS, the receivers must be low in radioactivity, and (b) their enclosure material should be compatible with the LS for 20 years. The details on how these two requirements are to be addressed will be discussed in a separate paper, and we shall primarily focus on the position accuracy herein.

## 3 Conceptual design

As mentioned above, an ultrasonic emitter is attached to the radioactive source. An array of ultrasonic receivers is placed on the inner surface of the CD. The emitter is driven from the outside, and the starting time is exactly known. The time of flight of the arrival signal on each ultrasonic receiver is used to calculate the distance between the emitter and receiver. Assuming a receiver array with no less than three sensors, the vertex location can be reconstructed through the geometric relationship [15, 16]. To be explicit, let the coordination of each receiver be  $(x_i, y_i, z_i)$ ,  $i = 1, 2, 3, 4$ , and  $T(X, Y, Z)$  is the coordinate of the emitter. Subsequently, the distance–time constraints can be written as

$$(X - x_i)^2 + (Y - y_i)^2 + (Z - z_i)^2 = (ct_i)^2, \quad i = 1, 2, 3, 4, \quad (1)$$

where  $c$  is the speed of sound in water and  $t_i$  is the TOF for each receiver [17, 18].

Using the cube array as an example [19–21], with the four sensor positions at  $A(0, 0, 0)$ ,  $B(L, 0, 0)$ ,  $C(0, L, 0)$ ,  $D(0, 0, L)$  in the Cartesian space, the position coordinate  $X$  of the emitter (the remainder of the coordinates are similar) is as follows:

$$X = \frac{1}{2L} (r_A^2 - r_B^2 + L^2) = \frac{1}{2L} [(t_{AC})^2 - (t_{BC})^2 + L^2], \quad (2)$$

with its uncertainty

$$\begin{aligned}
 dX &= \frac{1}{2L} [2ct_A(t_A dc + c dt_A) - 2ct_B(t_B dc + c dt_B)] \\
 &= \frac{1}{L} (r_A t_A - r_B t_B) dc + \frac{c}{L} (r_A dt_A - r_B dt_B)
 \end{aligned}
 \tag{3}$$

where  $r_A$  and  $r_B$  are the distances of the emitter to receivers  $A$  and  $B$ , respectively. As shown, the error consists of the sound speed measurement uncertainty,  $dc$  and two time measurement uncertainties,  $dt_A$  and  $dt_B$  [22–24].

In Fig. 2, the sound speed in the LS (linear alky benzene) is measured as a function of the liquid temperature. The operation temperature of the JUNO LS is expected to be  $21 \pm 1$  °C. An accurate measurement of the temperature profile to  $0.1^\circ$  would lead to a maximum average sound speed bias of 0.4 m/s. With the maximum emitter–receiver separation of 35 m, this translates into an uncertainty of 0.03% in distance. Meanwhile, the time-of-flight measurement uncertainty is dominated by the clock cycle uncertainty and the pulse rising edge measurement uncertainty (related to the signal-to-noise ratio) [25–27]. For a typical ultrasonic frequency of 150 kHz (sine wave pulses), the time measurement accuracy can easily reach one cycle (7  $\mu$ s). Under these assumptions, the typical uncertainty to  $dX$  can reach 1.6 cm.

The conceptual design of the full positioning system is depicted in Fig. 3. An array consists of eight receivers arranged in an inscribed cube on the CD wall. The position of the emitter can be calculated by any three receivers that are not in the same plane using the algorithm above. Therefore, an array of eight would exhibit redundancy to ensure the accuracy.

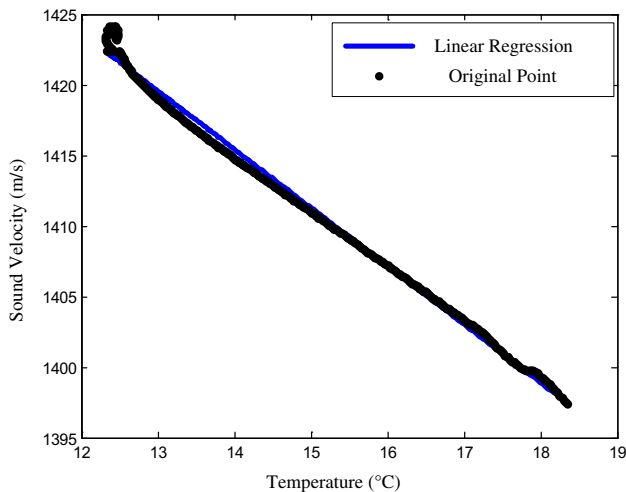


Fig. 2 Speed of ultrasonic sound in LS, measured by CTD from AML company

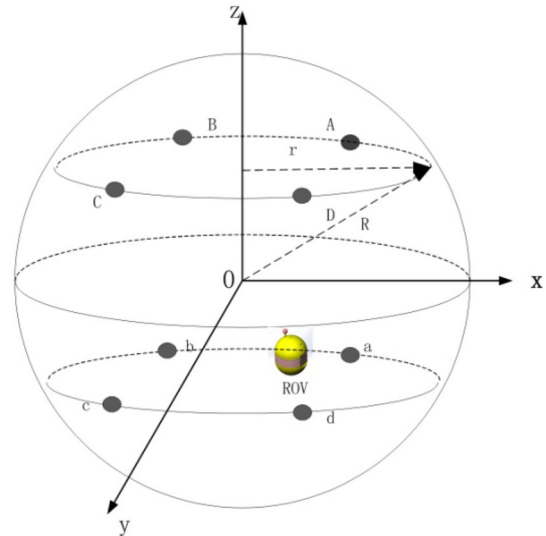


Fig. 3 Diagram of the cubic array

#### 4 The implementation of a prototype positioning system

The wiring diagram of a complete system, including the ultrasonic emitter, receivers, and the control and data acquisition system, is depicted in Fig. 4.

The emitter contains a piezoelectric core that converts the driving electrical signals, provided by the interface extension, to physical vibrations. The emitter is spherical,

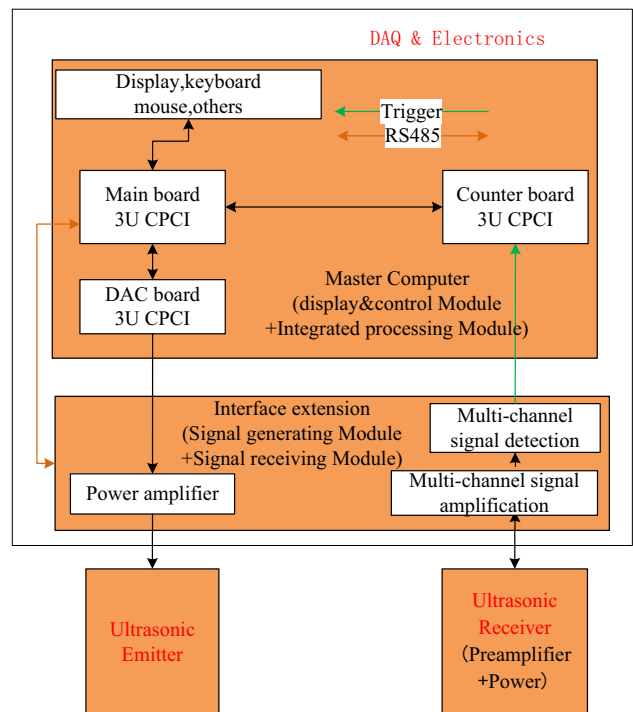


Fig. 4 (Color online) The hardware composition of the ultrasonic positioning system

as shown in Fig. 5a, which allows an omnidirectional emission. It operates at 150 kHz with almost a uniform generation ratio for a  $4\pi$  space. During operation, we placed the emitter within 10 cm to a PMT and observed no electromagnetic pickup from the PMT.

The receiver (Fig. 5b), also operating at 150 kHz, uses the same piezoelectric material to convert the received ultrasonic signals to electrical signals and sends them to the interface extension after the primary amplification. The receiver has uniform detection efficiency for a  $2\pi$  space.

The data acquisition and electronics comprise the master computer (backend) and front-end electronics. The master computer implements the display, task control, and integrated processing tasks. As the data processing and command center, its primary goal is to achieve the real-time calculation and display of the emitter position.

The front end (Fig. 5c) is a custom-made acoustic positioning board that implements the signal generation and receiving tasks. The signal-generating module handles the power amplification and synchronization of the emitting signals. The signal-receiving module performs multi-channel filtering, amplification, and signal detection. The eight receivers are synchronized by eight same-length cables connected to the signal-receiving modules. After detection, the signal-receiving module sends the trigger pulses corresponding to each channel to the master computer.

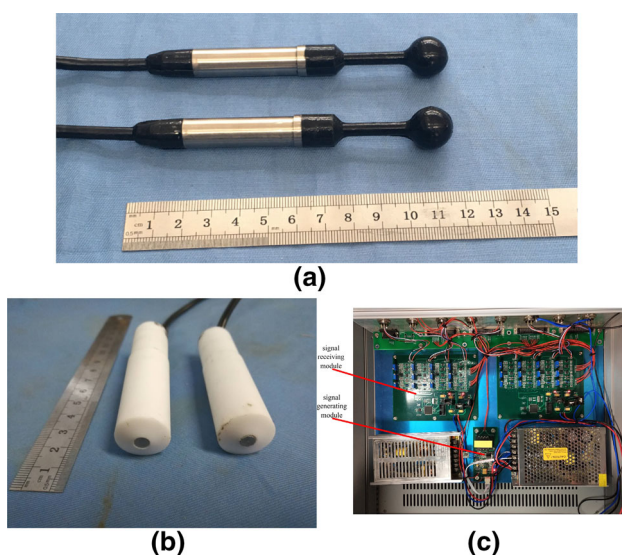


**Fig. 5** (Color online) **a** Picture of two prototype emitters. **b** Picture of two receivers. **c** The front-end board

## 5 Prototype performance

To verify the positioning accuracy of the ultrasonic positioning system, we performed the demonstration experiment in an anechoic water pool. The water pool is 20 m long, 8 m wide, and 7 m deep, and is surrounded by the anechoic wedges to avoid sound reflection in limited space. During the test, eight ultrasonic receivers are placed in a 5 m ( $L$ )  $\times$  5 m ( $W$ )  $\times$  4 m ( $H$ ) space as shown in Fig. 6. The emitter, attached to a solid steel bar, was moved around within the array space, with its location known to a precision of within a few centimeters. For each location, we compared the reconstructed positions with the true locations from the ultrasonic system.

### 5.1 Experimental setup

To affix the receivers, a steel cross with four arms was machined, as shown in Fig. 7a. The ultrasonic receivers were mounted at the end of each arm, with the upper four receivers attached rigidly, and the lower four receivers hanging below with fishing wires. The coordinate of each receiver was previously measured before the deployment of the array.

Nine holes with a separation of 25 cm in between were machined on each arm of the cross. In the experiment, the emitter was mounted below each hole with a fixed distance using a fishing cable; therefore, the true position was known to a precision of a few centimeters. A flange that was placed at the center of the cross allowed its attachment to the crane while maintaining itself leveled. The deployment of the array into water is illustrated in Fig. 7b.

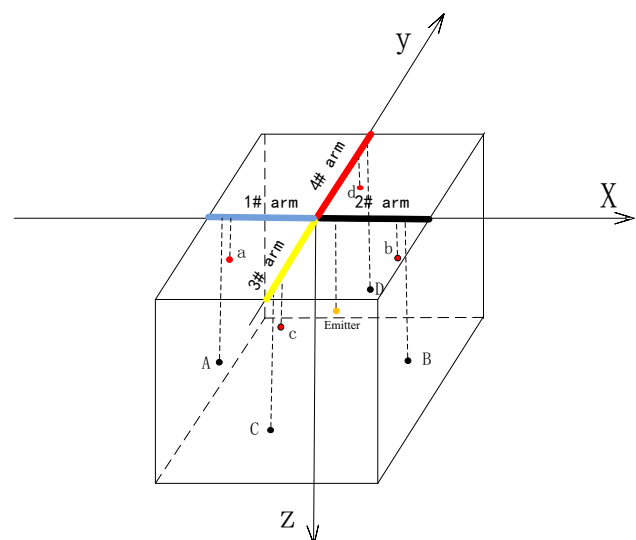
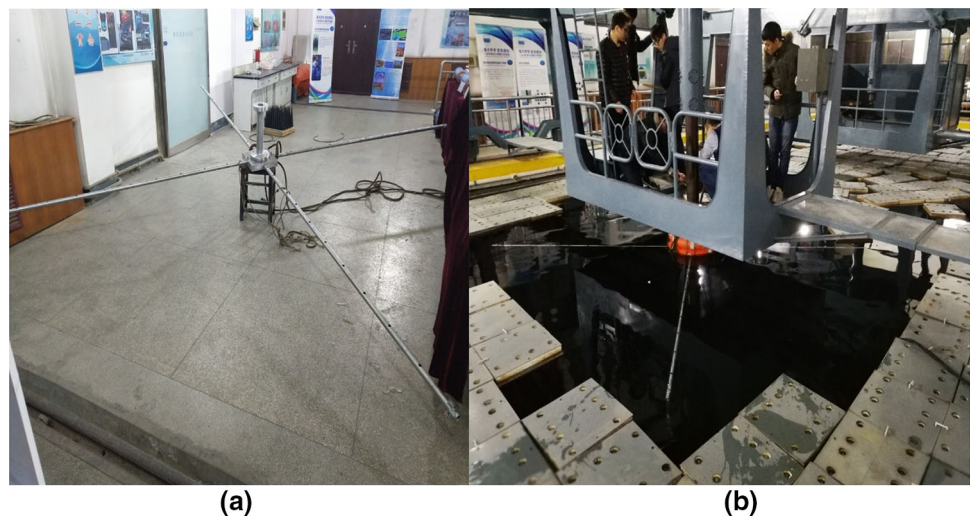


**Fig. 6** The diagram of the prototype receiver array

**Fig. 7** (Color online) **a** The receiver “cross.” **b** Deploying the array into the water



**5.2 Performance**

During operation, the ultrasonic emitter was driven by 15-cycle sine wave pulses with a width of 100  $\mu$ s, as shown by the yellow line in Fig. 8a. The typical signal received by the ultrasonic receivers is illustrated by the green line in Fig. 8b, where the waveform is somewhat distorted. We first obtain the envelope of the received waveform and measure the peak value of the envelope; subsequently, we use half the peak value as the detection threshold. The moment of over detection threshold is the moment when the signal is received, at which we can obtain the time-of-flight between the emitter and receiver.

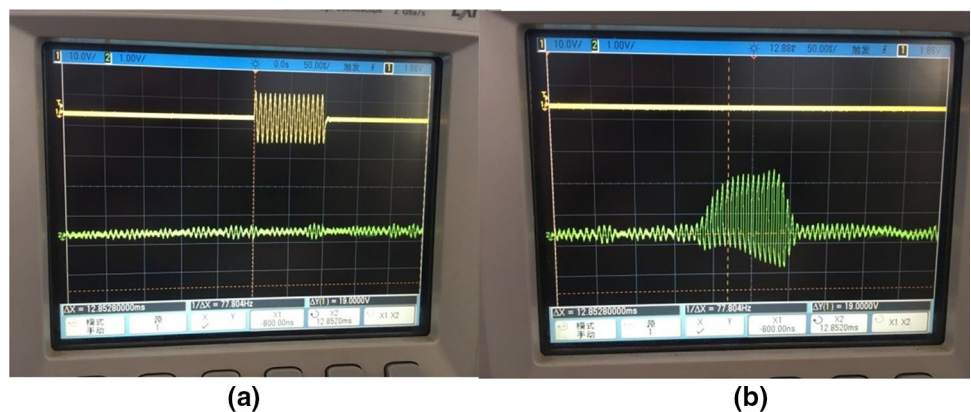
In the experiment, the ultrasonic emitter was placed at three different depths along one arm of the cross. At each depth ( $z \cong -150$  cm,  $-230$  cm, and  $-360$  cm), we scanned over seven positions. This procedure is illustrated in Fig. 9a. The locations of the eight receivers are shown as the black squares. The blue circles show the positions reconstructed by the ultrasonic receivers, and the red circles represent their true positions in three dimensions.

For each location, we repeated the positioning measurements ten times. The average values of  $x$ ,  $y$ , and  $z$  were used as the final reconstructed position. The repeatability was studied using the distance between the position given by each individual measurement and the averaged one. The results for all 21 positions are shown in Fig. 9b. The overall repeat uncertainty is approximately 1 mm (the dashed green line in Fig. 9b shows the average difference), and the maximum is less than 2.5 mm.

The differences in the reconstructed and true positions are calculated in all three axes. The deviation in the vertical direction shows an interesting trend (see Fig. 10a). The data become more scattered in the deeper location when the emitter was moved closer to the lower array. This reflects two potential effects. First, if the emitter is too close to a receiver plane, the relative accuracy in this dimension is degraded. Second, the cross could have some distortions under gravity that could lead to an increase in the vertical position uncertainty for larger radii.

We evaluated the distance between the reconstructed and true positions for all 21 points. As shown in Fig. 10b, the maximum difference in the point-by-point uncertainty

**Fig. 8** (Color online) **a** Driving pulse for emitter. **b** Signal received by receiver



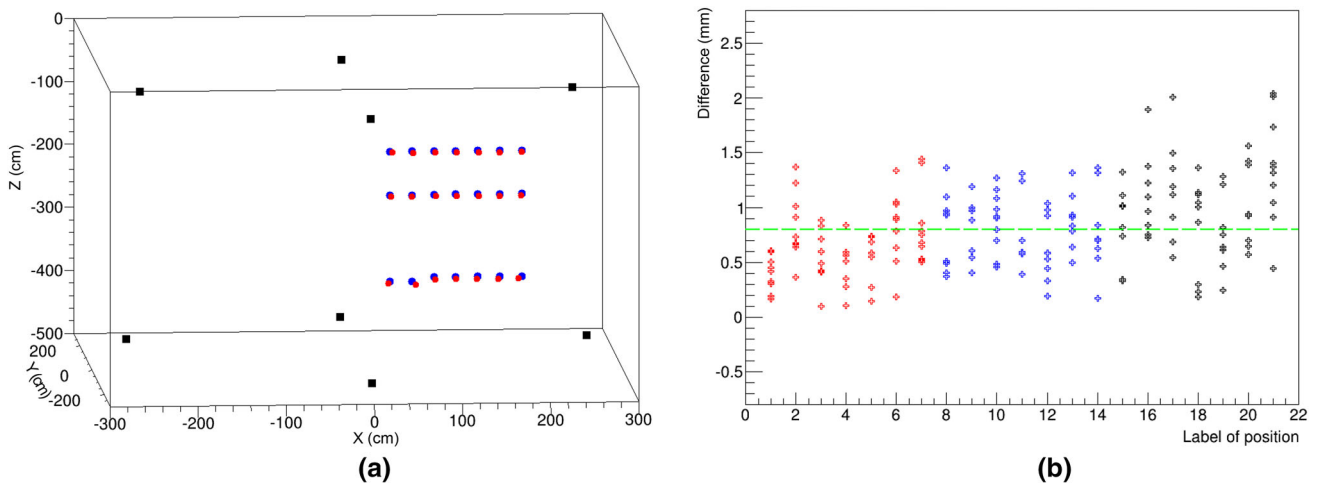


**Fig. 9** (Color online) **a** The experimental results: the black squares are the locations of the eight receivers, blue circles are the positions reconstructed by the ultrasonic receivers, and red circles are their true positions. **b** The repeatability of the positioning, measured by the difference between each measurement and the average: red points are

for the positions with  $Z \sim 150$  cm, blue ones are for  $Z \sim 230$  cm, and black ones are for  $Z \sim 360$  cm. X axis represents the measured positions (1–21) and Y axis represents the distance between each individual measurement and the average value

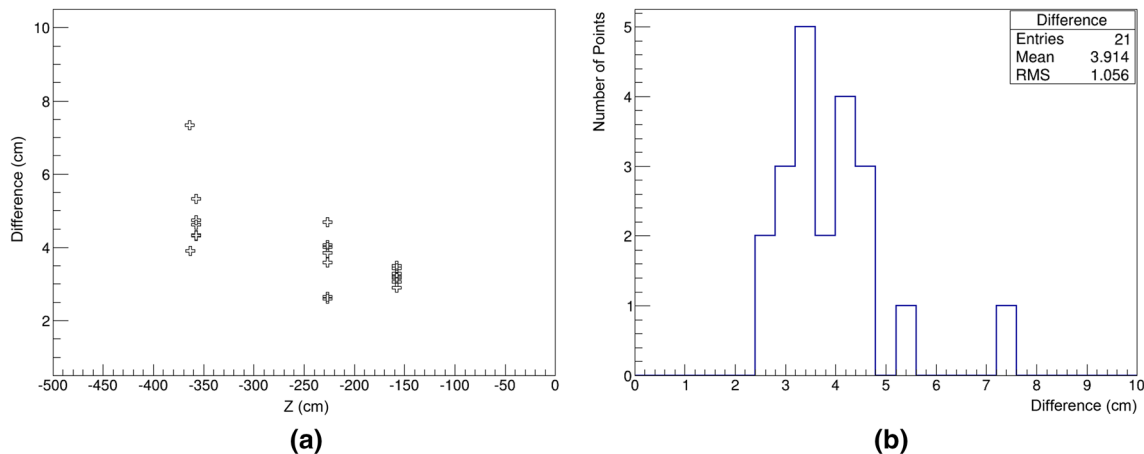


**Fig. 10** (Color online) **a** The difference between reconstructed and true positions in Z coordinate. X axis is the Z position (depth) of the measured points, and Y axis is the distance between the reconstructed

and true positions. **b** The distance between the true and reconstructed positions for all 21 points. X axis is the distance between the reconstructed and true positions

is 7.3 cm, and two point differences are larger than 5 cm. The mean value of the uncertainty for all 21 points is 3.9 cm. In the future, we hope to reduce the maximum difference to less than 4 cm.

### 5.3 Discussions

The uncertainty of the reconstruction could be due to the following factors. (1) Receiver position uncertainty. During the prototype test, because the lower four receivers were hung onto the cross via fishing cables, the exact location of the receiver under water could accommodate a bias of up to a few centimeters. (2) Emitter true position uncertainty. The emitter was hung onto the cross via a fishing cable;

therefore, a potential bias of an order of centimeter under water is also possible. It is noteworthy that owing to the limited size of the array, a small positioning uncertainty owing to the emitter and receiver translates to a larger fraction uncertainty to the reconstructed position. (3) Temperature effect. The water temperature between the upper and lower arrays differed by approximately  $1^\circ$ . Assuming (conservatively) a bias of 4 m/s in the sound speed, in 10 m, this corresponds to a bias of approximately 3 cm. (4) Trigger uncertainty. During the test, the front-end board determined the signal arrival timing based on the rising edge of the first cycle of the pulse, which could be sensitive to the noise level. As 15 cycles of the sine wave are present in each pulse, a more accurate determination of

the trigger time is possible. In the follow-up study, we will optimize the experimental conditions to continue minimizing the uncertainties.

## 6 Conclusion

A novel high-precision ultrasonic source positioning system was developed for the JUNO, to simultaneously satisfy the positioning accuracy, robustness, and compatibility with the PMT operation. A realistic prototype system was constructed and tested; it could reconstruct the source position within a 4-cm accuracy and up to 1-mm repeatability within a 5 m ( $L$ )  $\times$  5 m ( $W$ )  $\times$  4 m ( $H$ ) range. Further optimization is ongoing to improve the system performance.

## References

1. T. Adam, F. An, G. An et al. (JUNO collaboration), in *JUNO Conceptual Design Report*, arXiv:1508.07166 (2015)
2. F.P. An, G.P. An, Q. An et al., (JUNO Collaboration), Neutrino physics with JUNO. *J. Phys. G: Nucl. Part. Phys.* **43**, 030401 (2016). <https://doi.org/10.1088/0954-3899/43/3/030401>
3. L. Zhan, Y.F. Wang, J. Cao et al., Determination of the neutrino mass hierarchy at an intermediate baseline. *Phys. Rev. D* **78**, 111103(R) (2008). <https://doi.org/10.1103/PhysRevD.78.111103>
4. Y.F. Li, J. Cao, Y.F. Wang et al., Unambiguous determination of the neutrino mass hierarchy using reactor neutrinos. *Phys. Rev. D* **88**, 013008 (2013). <https://doi.org/10.1103/PhysRevD.88.013008>
5. X.C. Ye, B.X. Yu, X. Zhou et al., Preliminary study of light yield dependence on LAB liquid scintillator composition. *Chin. Phys. C* **39**, 096003 (2015). <https://doi.org/10.1088/1674-1137/39/9/096003>
6. X. Zhou, Q.M. Zhang, Q. Liu et al., Densities, isobaric thermal expansion coefficients and isothermal compressibilities of linear alkylbenzene. *Phys. Scr.* **90**, 055701 (2015). <https://doi.org/10.1088/0031-8949/90/5/055701>
7. Y.F. Wang, S. Qian, T. Zhao et al., A new design of large area MCP-PMT for the next generation neutrino experiment. *Nucl. Instrum. Methods A* **695**, 113–117 (2012). <https://doi.org/10.1016/j.nima.2011.12.085>
8. M. He, in *TIPP 2017 proceeding of Double Calorimetry System in JUNO*, arXiv:1706.08761 (2017)
9. L. Zhan, Y.F. Wang, J. Cao et al., Experimental requirements to determine the neutrino mass hierarchy using reactor neutrinos. *Phys. Rev. D* **79**, 073007 (2009). <https://doi.org/10.1103/PhysRevD.79.073007>
10. X. Qian, D.A. Dwyer, R.D. McKeown et al., Mass hierarchy resolution in reactor anti-neutrino experiments: parameter degeneracies and detector energy response. *Phys. Rev. D* **87**, 033005 (2013). <https://doi.org/10.1103/PhysRevD.87.033005>
11. J. Liu, B. Cai, R. Carr et al., Automated calibration system for a high-precision measurement of neutrino mixing angle  $\theta_{13}$  with the Daya Bay antineutrino detectors. *Nucl. Instrum. Methods A* **750**, 19–37 (2014). <https://doi.org/10.1016/j.nima.2014.02.049>
12. F.P. An, J.Z. Bai, A.B. Balantekin et al., (Daya Bay Collaboration), Observation of electron-antineutrino disappearance at Daya Bay. *Phys. Rev. Lett.* **108**, 171803 (2012). <https://doi.org/10.1103/PhysRevLett.108.171803>
13. M. Xiao, JUNO central detector and calibration strategy, talk on *International Workshop on Next Generation Nucleon Decay and Neutrino Detectors (NNN16)*
14. Q. Liu, M. He, X.F. Ding et al. in *A Vertex Reconstruction Algorithm in the Central Detector of JUNO*, arXiv:1803.09394
15. B. Møhl, M. Wahlberg, A. Heerfordt, A large-aperture array of nonlinked receivers for acoustic positioning of biological sound sources. *J. Acoust. Soc. Am.* **109**, 434–437 (2001). <https://doi.org/10.1121/1.1323462>
16. T. Tian, *Underwater positioning and navigation technology* (National Defence Industry Press, Beijing, 2007), pp. 20–21
17. H.S. Hashemi, H. Rivaz, Global time-delay estimation in ultrasound elastography. *IEEE Trans. Ultrason. Ferroelectr.* **64**, 1625–1636 (2017). <https://doi.org/10.1109/TUFFC.2017.2717933>
18. M. Georgiev, R. Bregovic, A. Gotchev, Time-of-flight range measurement in low-sensing environment: noise analysis and complex-domain non-local denoising. *IEEE Trans. Image Process.* **27**, 2911–2926 (2018). <https://doi.org/10.1109/TIP.2018.2807126>
19. J.F. Wang, N. Zou, F. Jin, Research on integrated positioning approach based on long/ultra-short baseline. *J. Acoust. Soc. Am.* **143**, 1958 (2018). <https://doi.org/10.1121/1.5036434>
20. Y. Watanabe, H. Ochi, T. Shimura, The study on data transmission with short positioning pulse in deep sea. *J. Acoust. Soc. Am.* **120**, 3049–3058 (2006). <https://doi.org/10.1121/1.4787261>
21. Z. Li, G. Qi, Z.X. Sun, A short baseline-based real-time high-precision ROV position system. *High Technol. Lett.* **23**(12), 1230–1235 (2013)
22. D.J. Thomson, S.E. Dosso, D.R. Barclay, Modeling AUV localization error in a long baseline acoustic positioning system. *IEEE J. Ocean. Eng.* **134**, 1–14 (2017). <https://doi.org/10.1109/JOE.2017.2771898>
23. X. Liu, N. Zou, Y. Zhang, Methods of unwrapping phase ambiguity and selecting direct sounds in an ultra short baseline positioning system. *J. Acoust. Soc. Am.* **142**, 2731 (2017). <https://doi.org/10.1121/1.5014978>
24. D. Sun, J. Gu, J. Zhang, et al. Design of high accuracy ultra short baseline underwater acoustic position system, in *IEEE International Conference on Signal Processing, Communications and Computing*. (Xiamen, China, 2017)
25. S. Zhao, C.J. Qiao, Y.K. Wang., On the navigation positioning technologies in AUV underwater docking, in *Proceedings of the 31st Chinese Control Conference*, (Hefei, China, 2012)
26. Y.Y. Wang, C.J. Qiao, S.Y. Liu. Design of autonomous underwater vehicle positioning system, in *2016 IEEE Advanced Information Management, Communicates, Electronic and Automation Control Conference (IMCEC)*, (Xi'an, China, 2016)
27. L. Paull, S. Saeedi, M. Seto et al., AUV navigation and localization: a review. *IEEE J. Ocean. Eng.* **39**(1), 131–149 (2014). <https://doi.org/10.1109/JOE.2013.2278891>